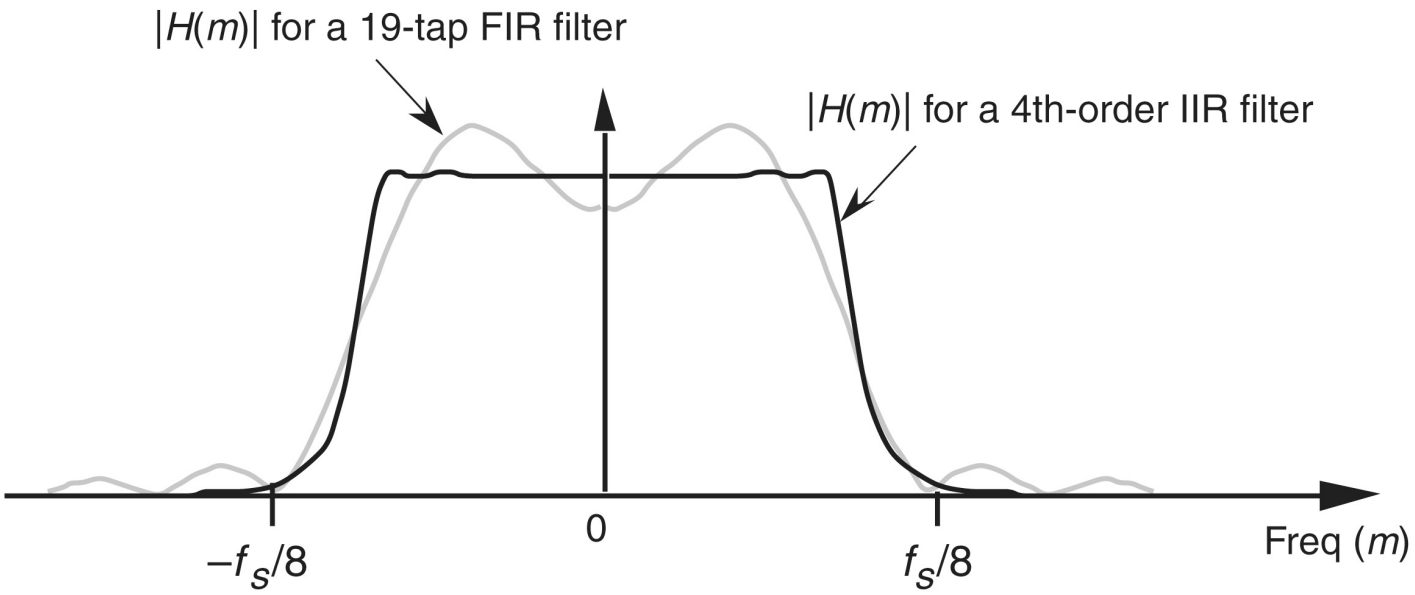

Figure 6–1 Comparison of the frequency magnitude responses of a 19-tap lowpass FIR filter and a 4th-order lowpass IIR filter.

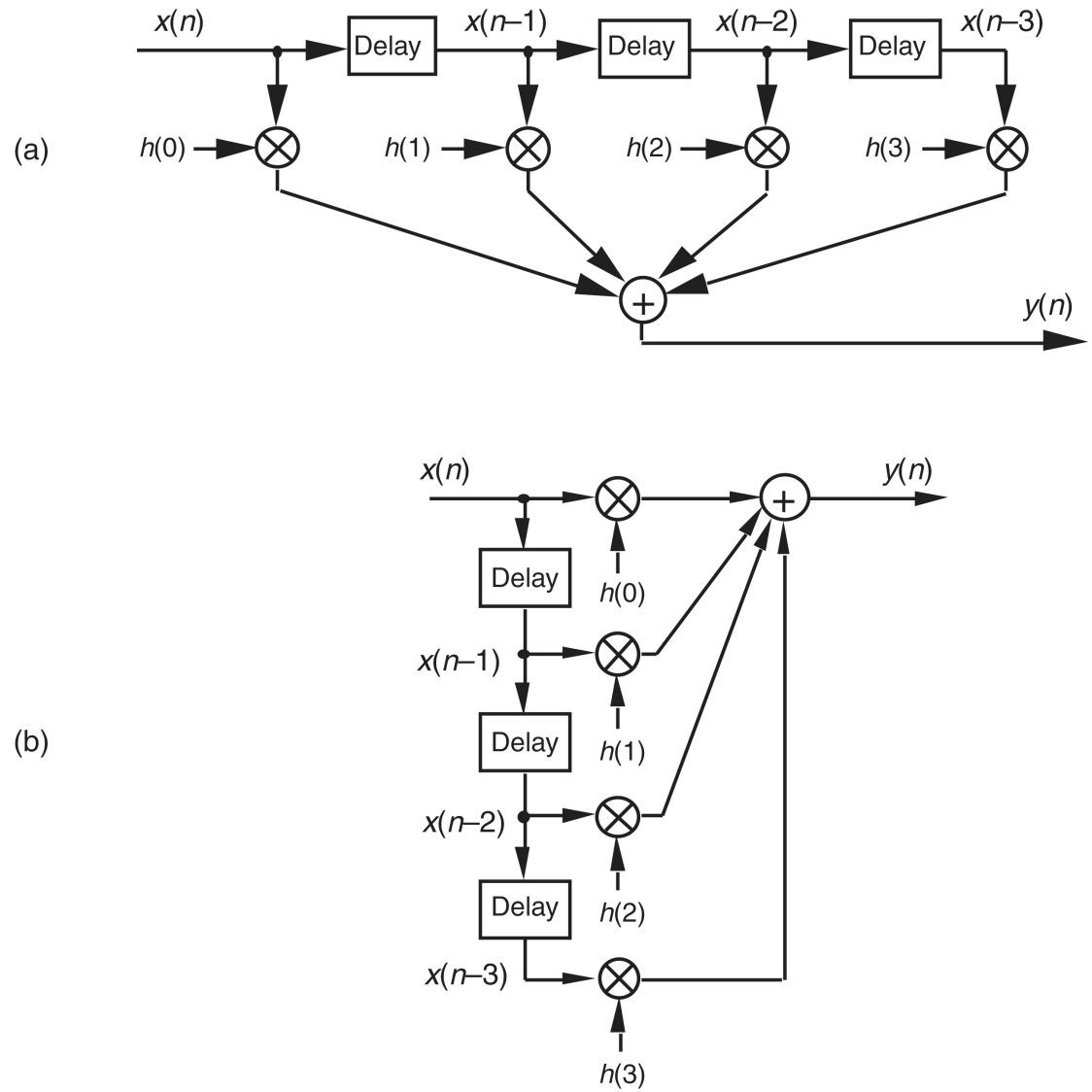

Figure 6–2 FIR digital filter structures: (a) traditional FIR filter structure; (b) re-arranged, but equivalent, FIR filter structure.

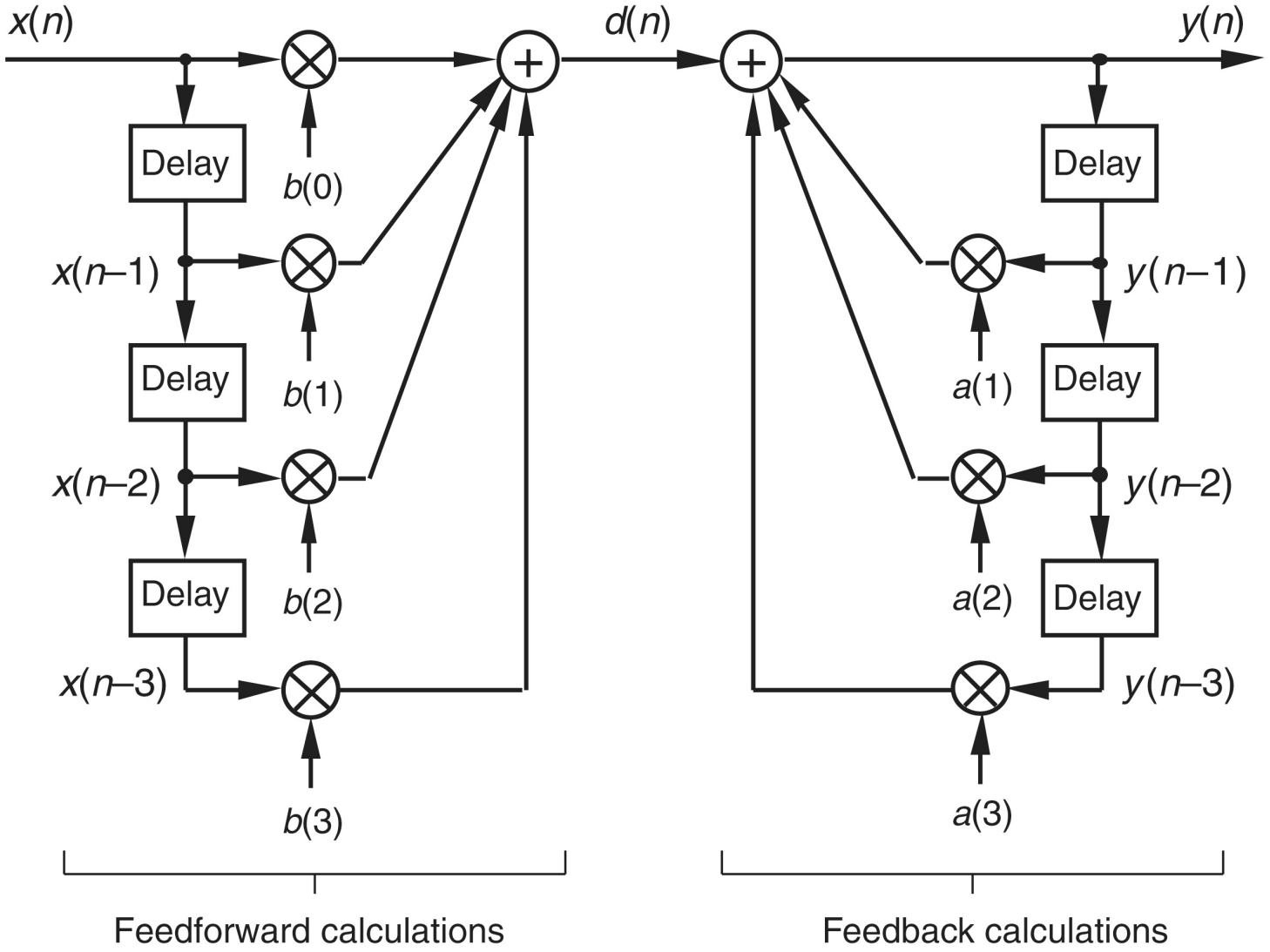

Figure 6–3 IIR digital filter structure showing feedforward and feedback calculations.

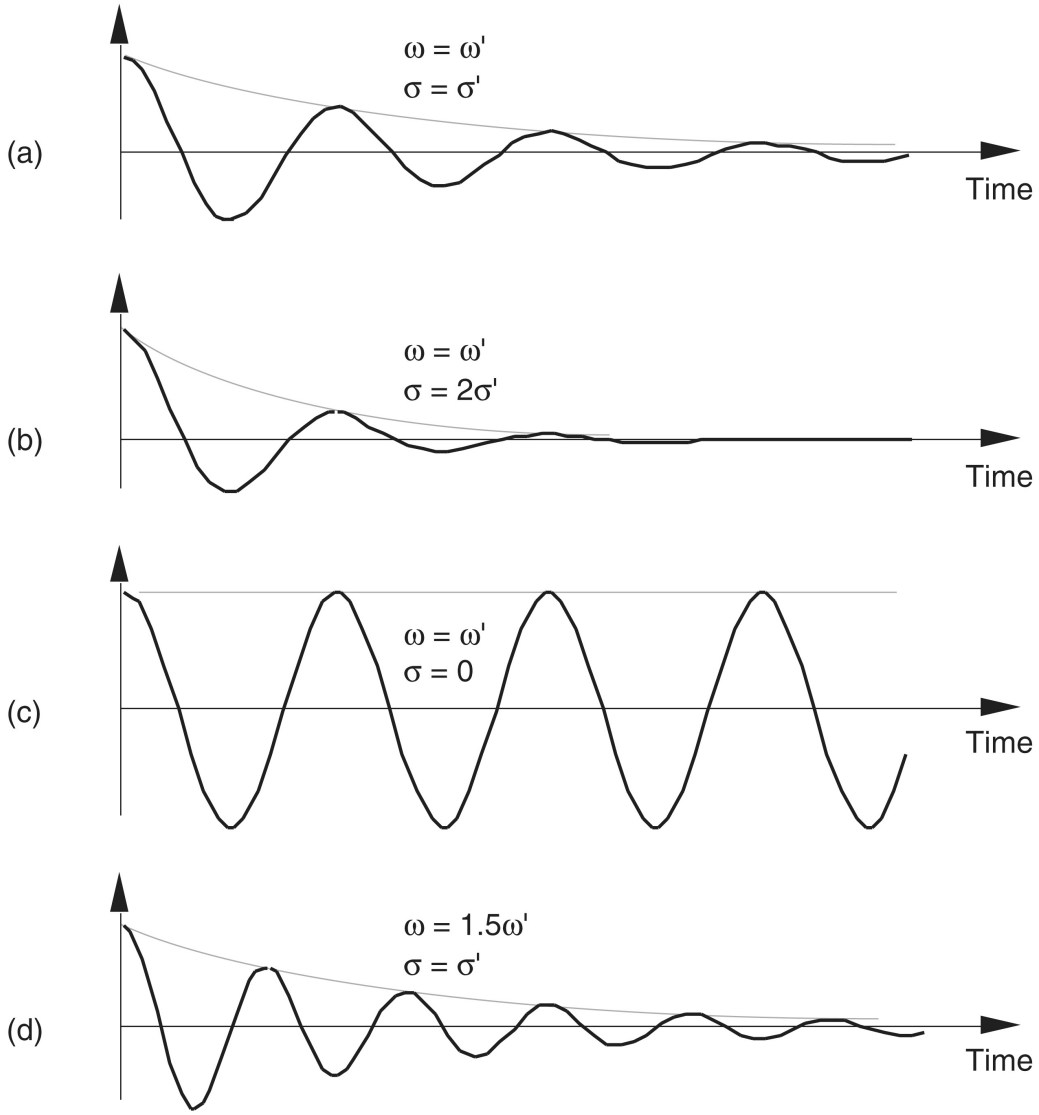

Figure 6–4 Real part (cosine) of various e^{-st} functions, where $s = \sigma + j\omega$, to be correlated with $f(t)$.

Figure 6–5 System described by Eq. (6–6). The system's input and output are the continuous-time functions $x(t)$ and $y(t)$ respectively.

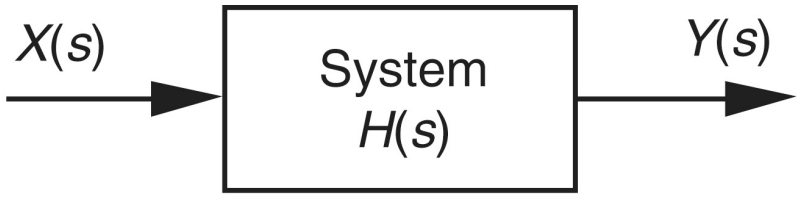

Figure 6–6 Linear system described by Eqs. (6–10) and (6–11). The system's input is the Laplace function $X(s)$, its output is the Laplace function $Y(s)$, and the system transfer function is $H(s)$.

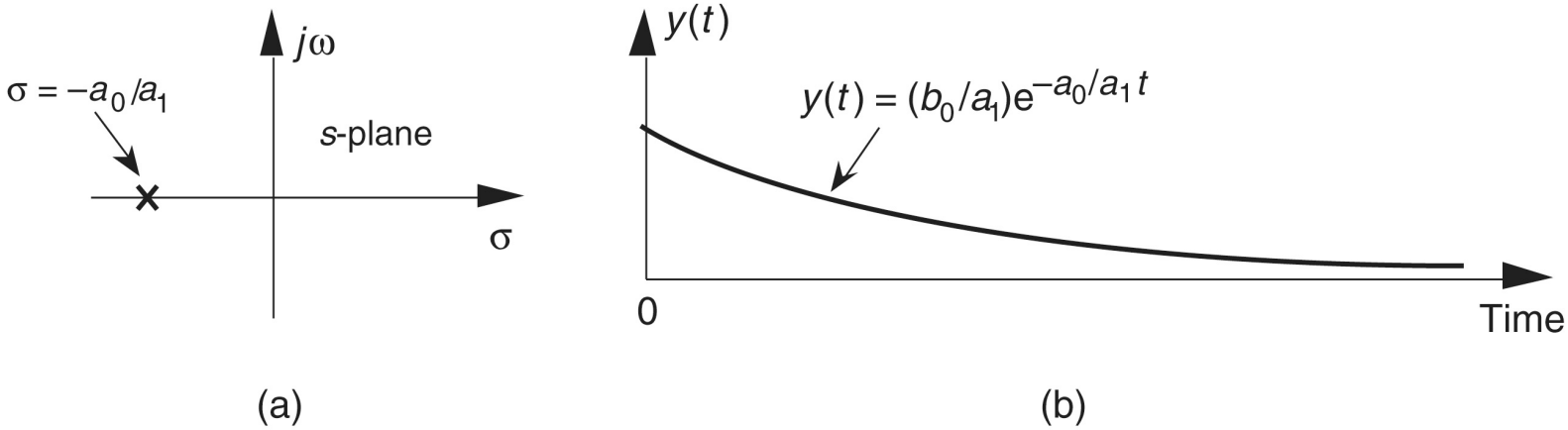

Figure 6–7 Descriptions of $H_1(s)$: (a) pole located at $s = \sigma + j\omega = -a_0/a_1 + j0$ on the s-plane; (b) time-domain $y(t)$ impulse response of the system.

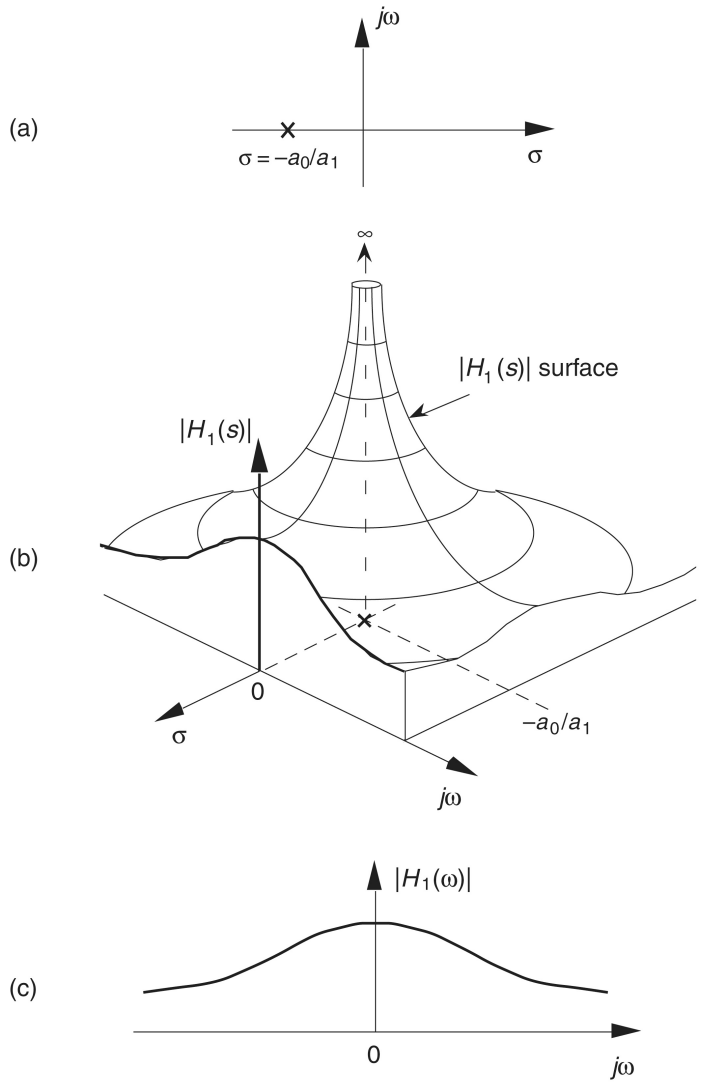

Figure 6–8 Further depictions of $H_1(s)$: (a) pole located at $\sigma = -a_0/a_1$ on the *s*-plane; (b) $|H_1(s)|$ surface; (c) curve showing the intersection of the $|H_1(s)|$ surface and the vertical $\sigma = 0$ plane. This is the conventional depiction of the $|H_1(\omega)|$ frequency magnitude response.

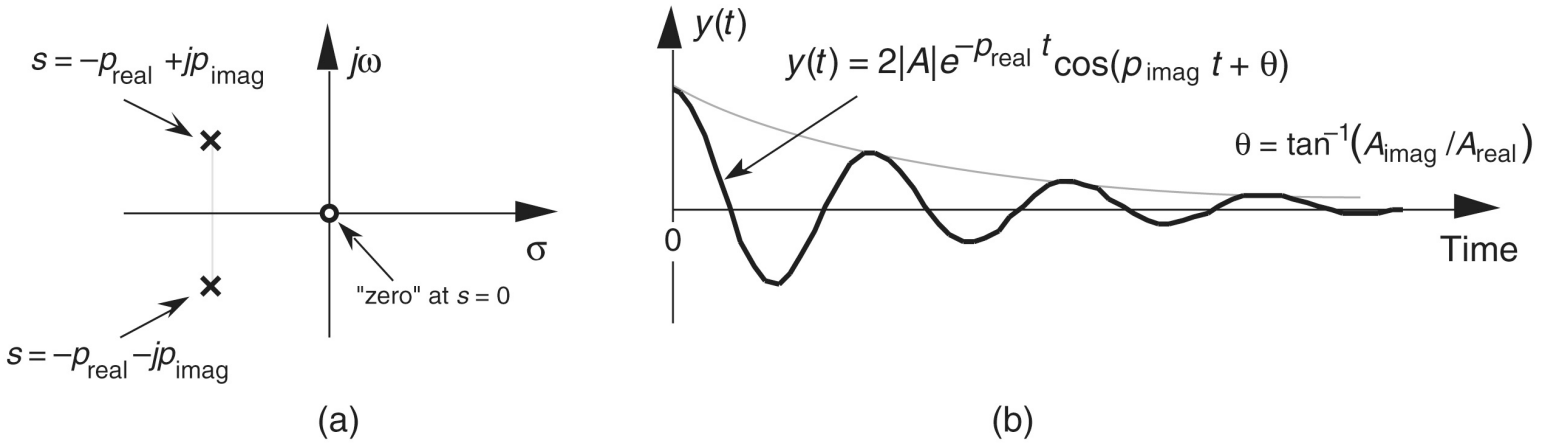

Figure 6–9 Descriptions of $H_2(s)$: (a) poles located at $s = p_{real} \pm jp_{imag}$ on the s-plane; (b) time-domain $y(t)$ impulse response of the system.

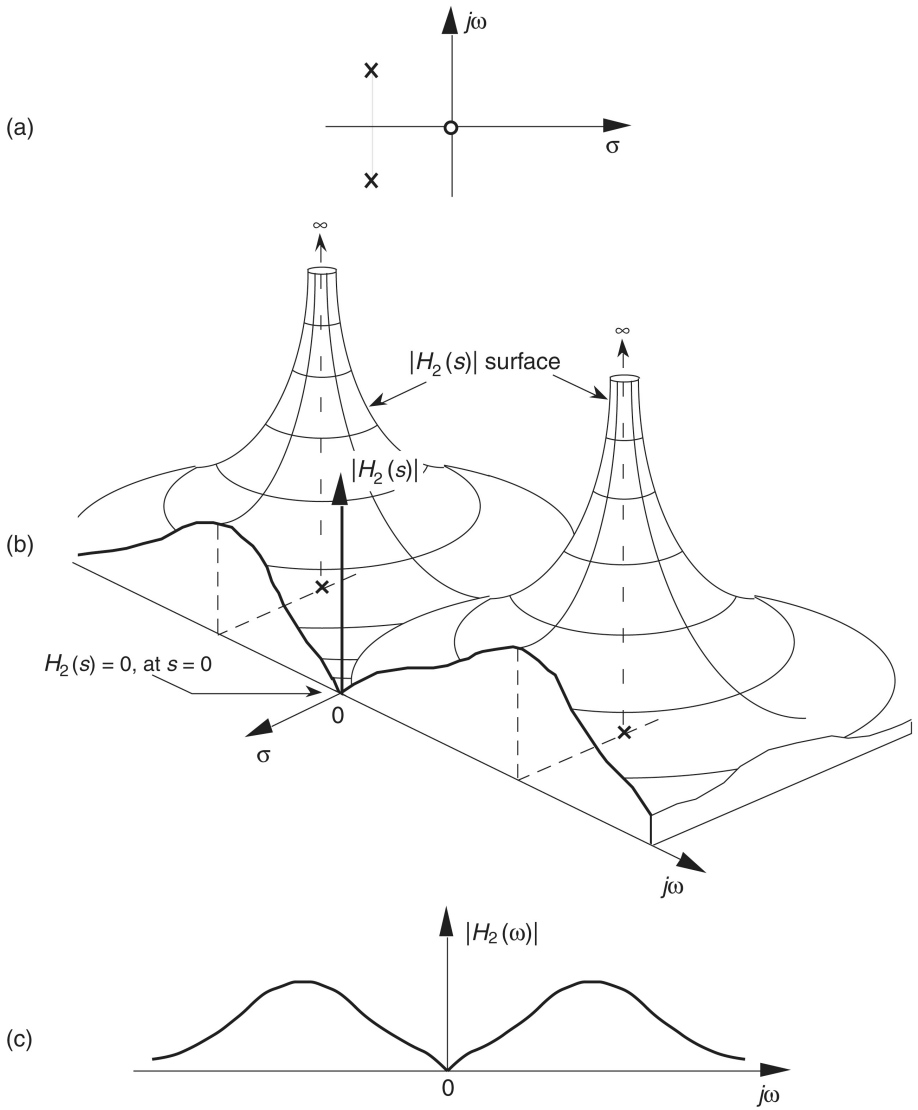

Figure 6–10 Further depictions of $H_2(s)$: (a) poles and zero locations on the *s*–plane; (b) $|H_2(s)|$ surface; (c) $|H_2(\omega)|$ frequency magnitude response curve.

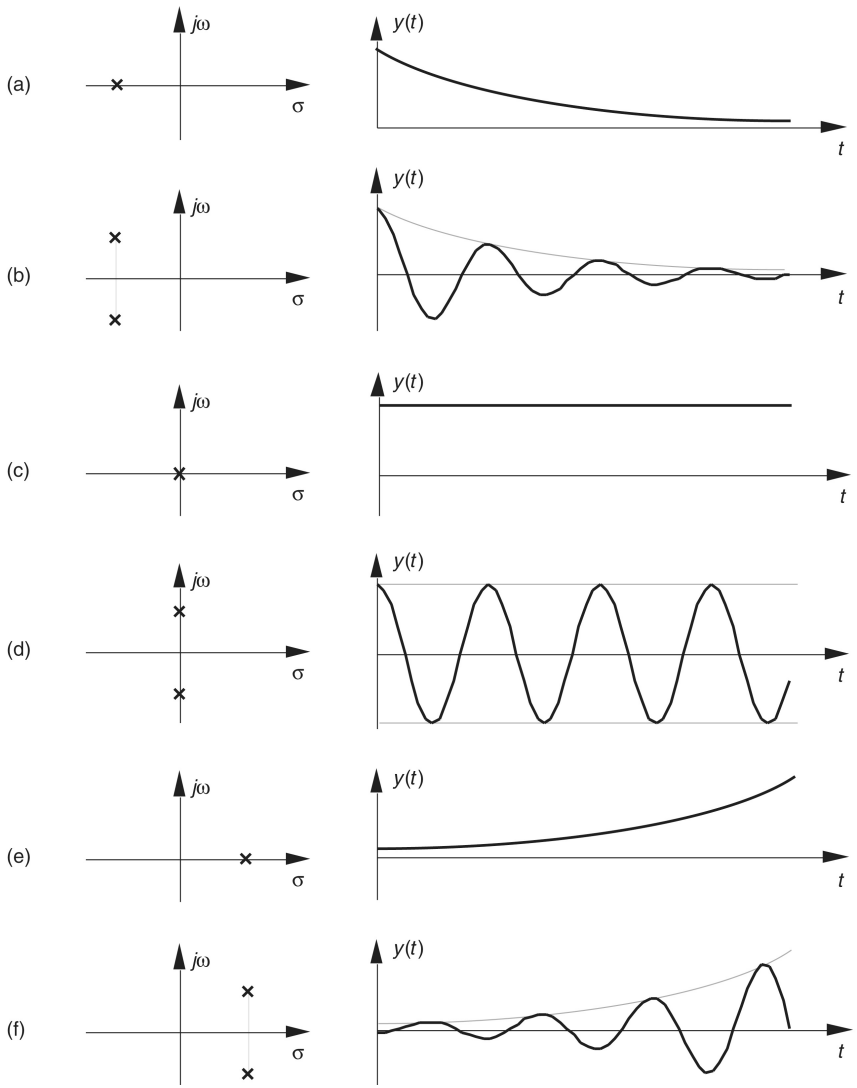

Figure 6–11 Various $H(s)$ pole locations and their time-domain impulse responses: (a) single pole at $\sigma < 0$; (b) conjugate poles at $\sigma < 0$; (c) single pole located at $\sigma = 0$; (d) conjugate poles located at $\sigma = 0$; (e) single pole at $\sigma > 0$; (f) conjugate poles at $\sigma > 0$.

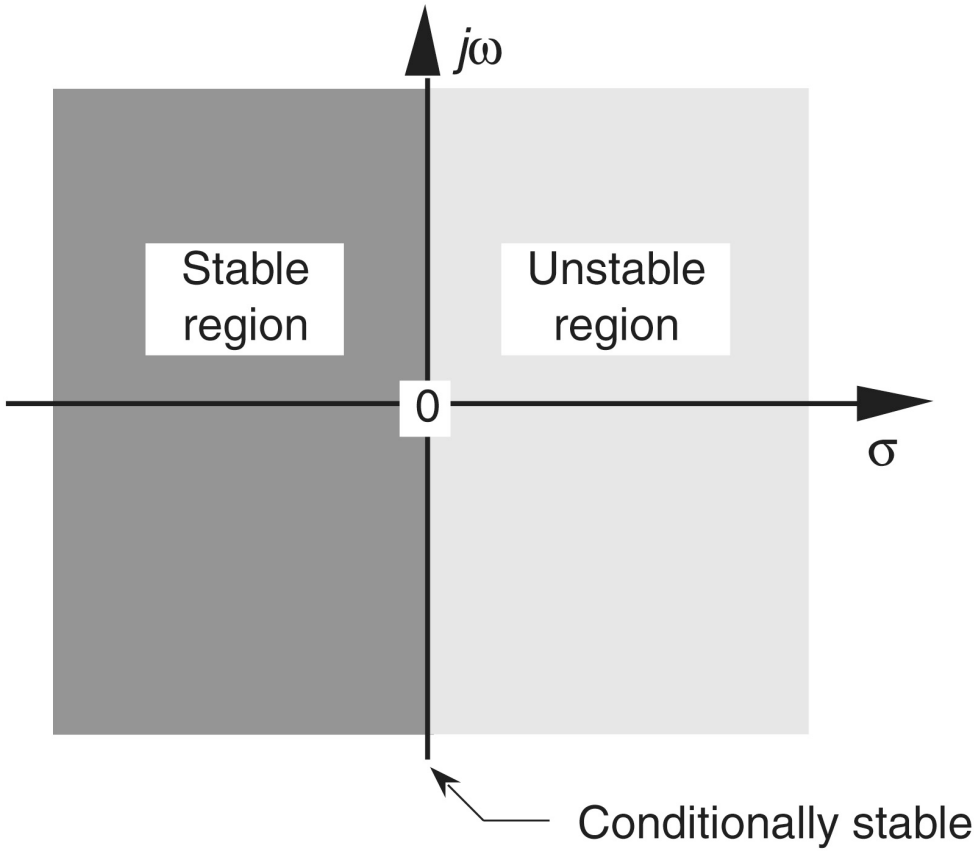

Figure 6–12 The Laplace *s–p*lane showing the regions of stability and instability for pole locations for linear continuous systems.

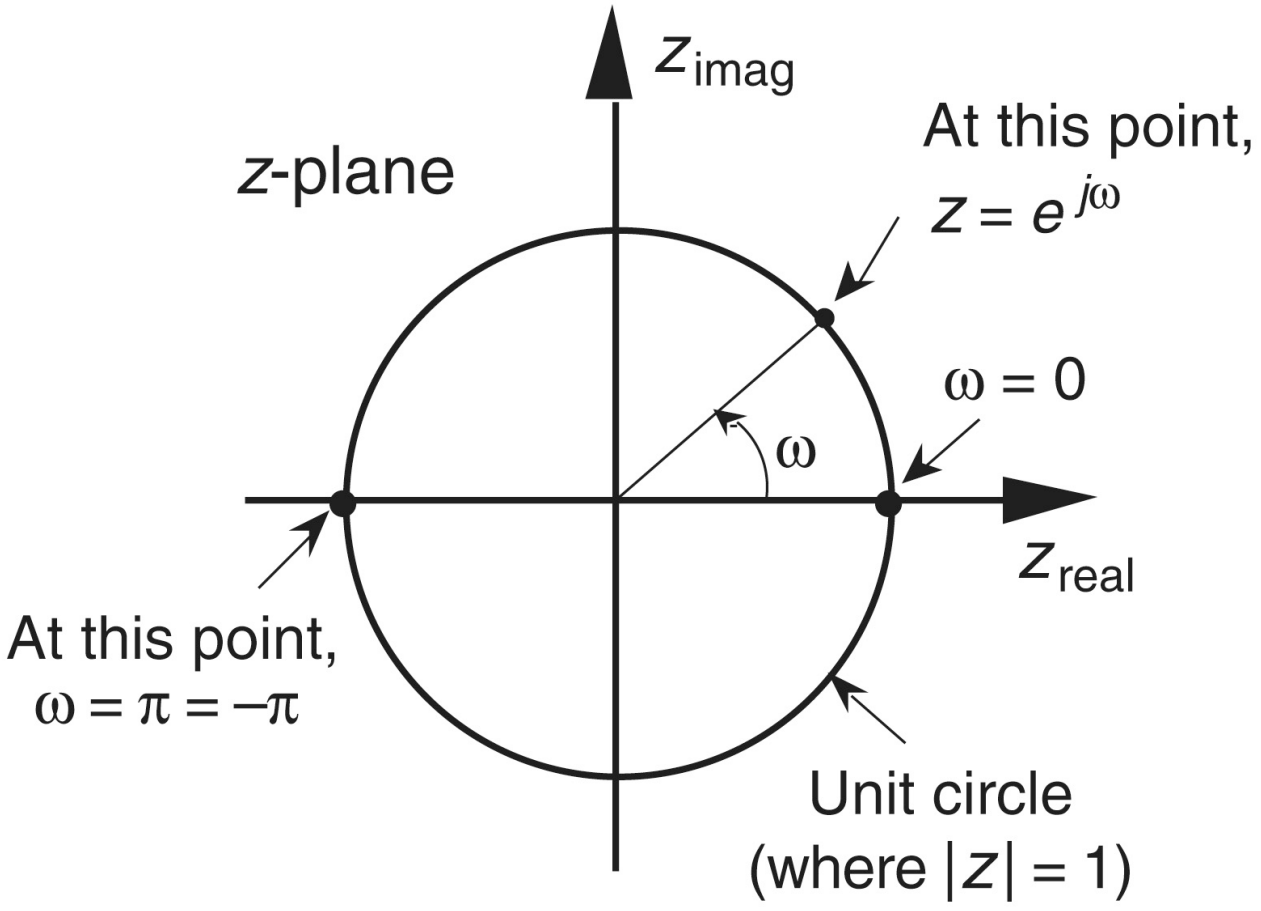

Figure 6–13 Unit circle on the complex *z*–plane.

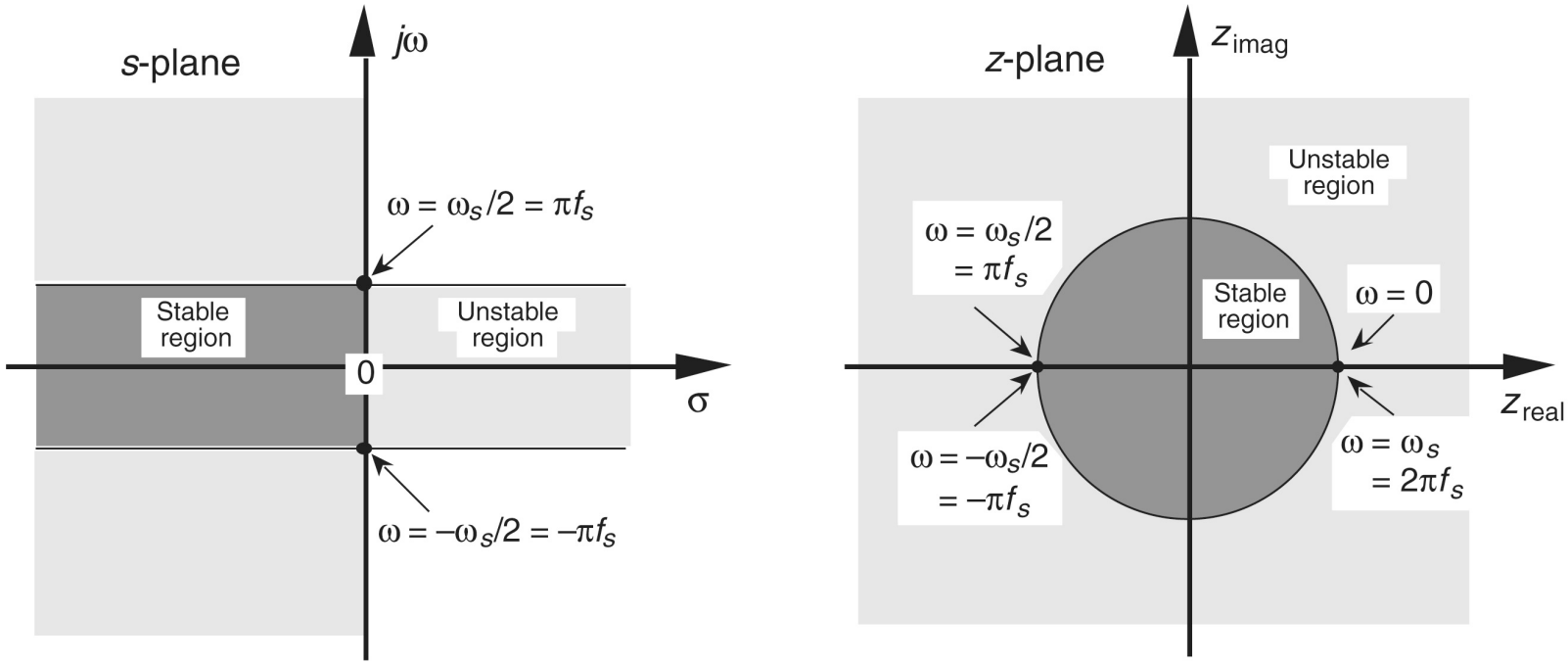

Figure 6–14 Mapping of the Laplace *s*–plane to the *z*–plane. All frequency values are in radians/second.

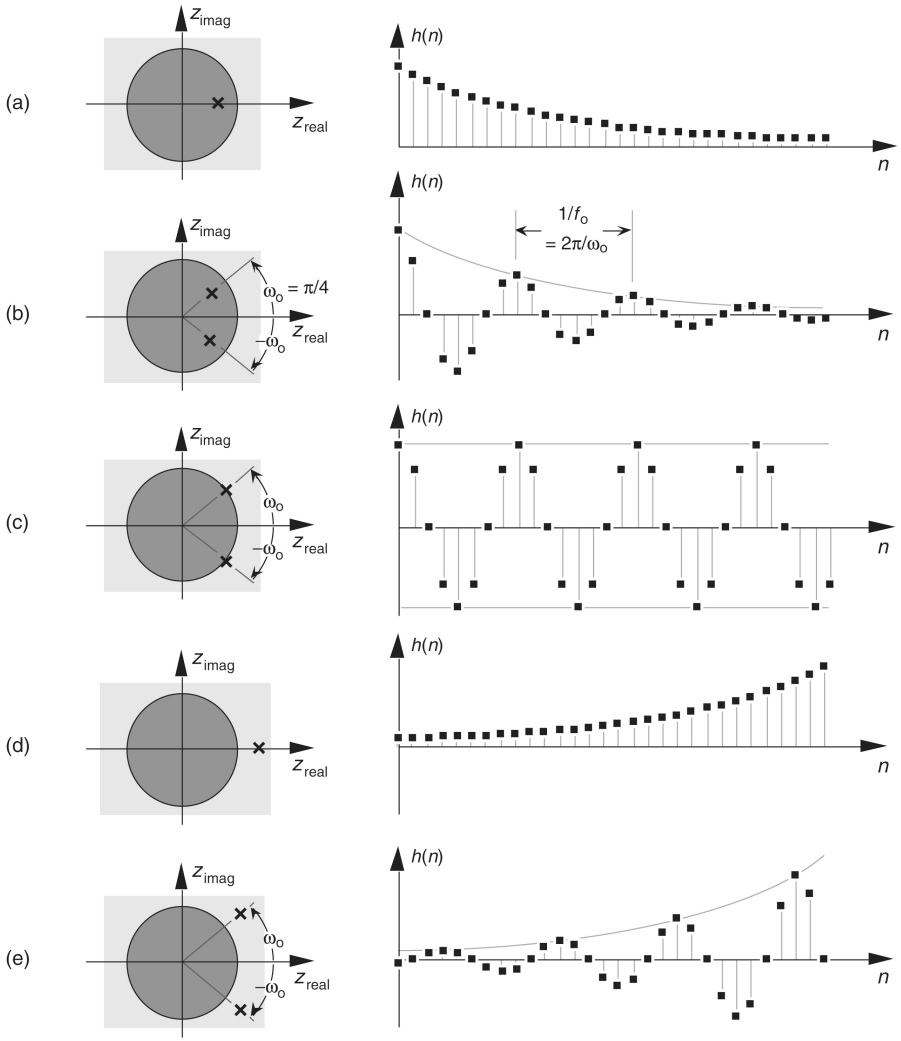

Figure 6–15 Various $H(z)$ pole locations and their discrete time-domain impulse responses: (a) single pole inside the unit circle; (b) conjugate poles located inside the unit circle; (c) conjugate poles located on the unit circle; (d) single pole outside the unit circle; (e) conjugate poles located outside the unit circle.

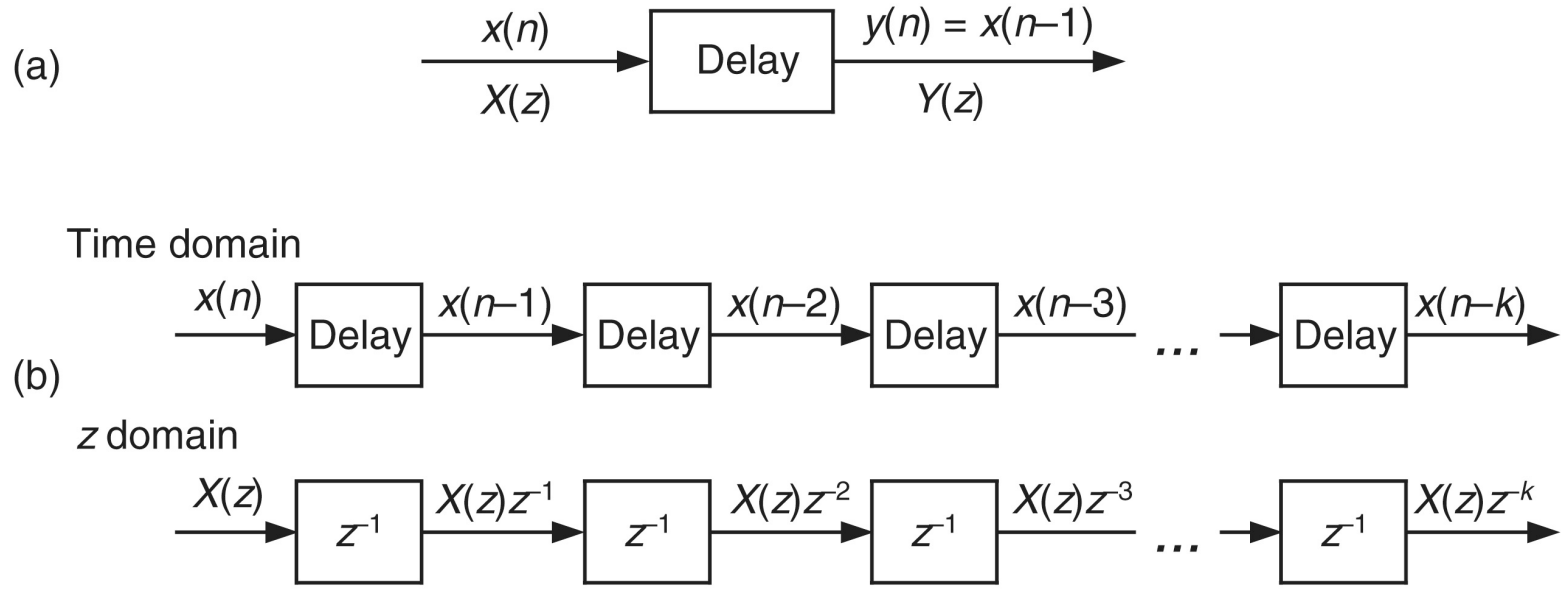

Figure 6–16 Time- and *z*-domain delay element relationships: (a) single delay; (b) multiple delays.

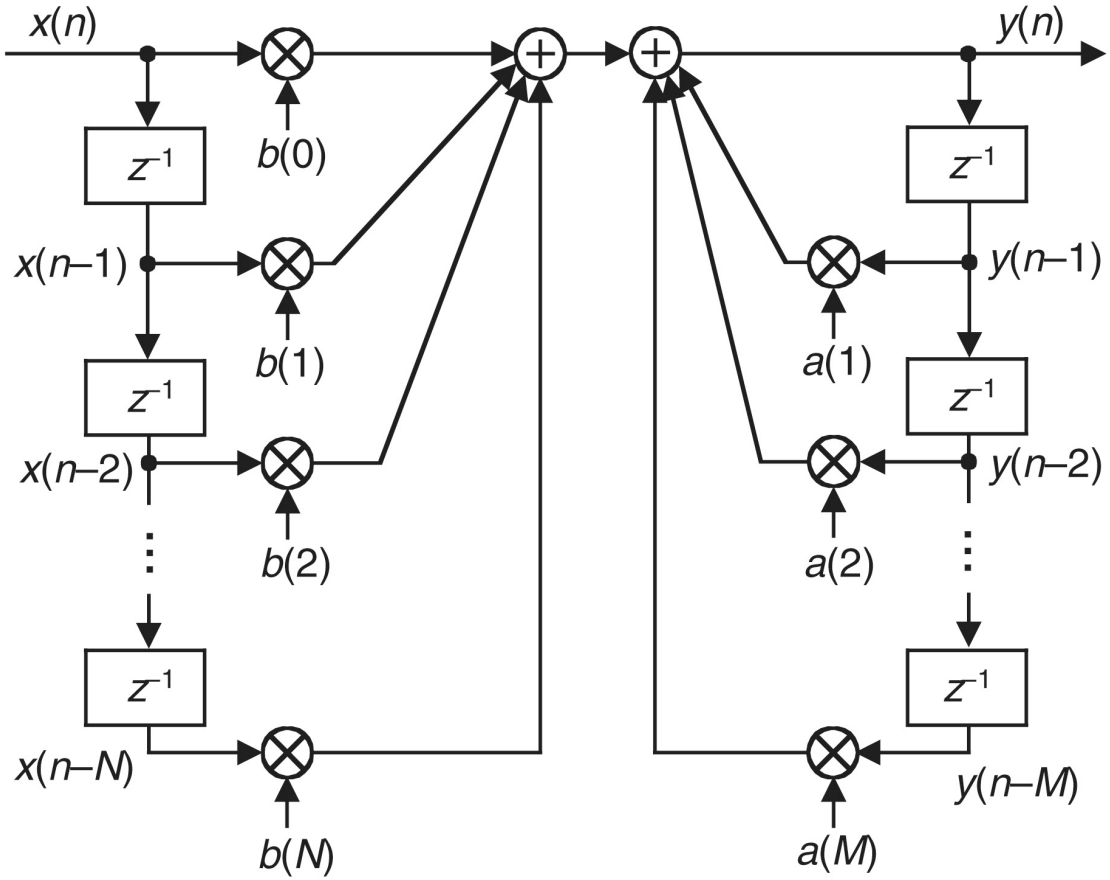

Figure 6–17 General (Direct Form I) structure of an *M*th-order IIR filter, having *N* feedforward stages and *M* feedback stages, with the z^{-1} operator indicating a unit time delay.

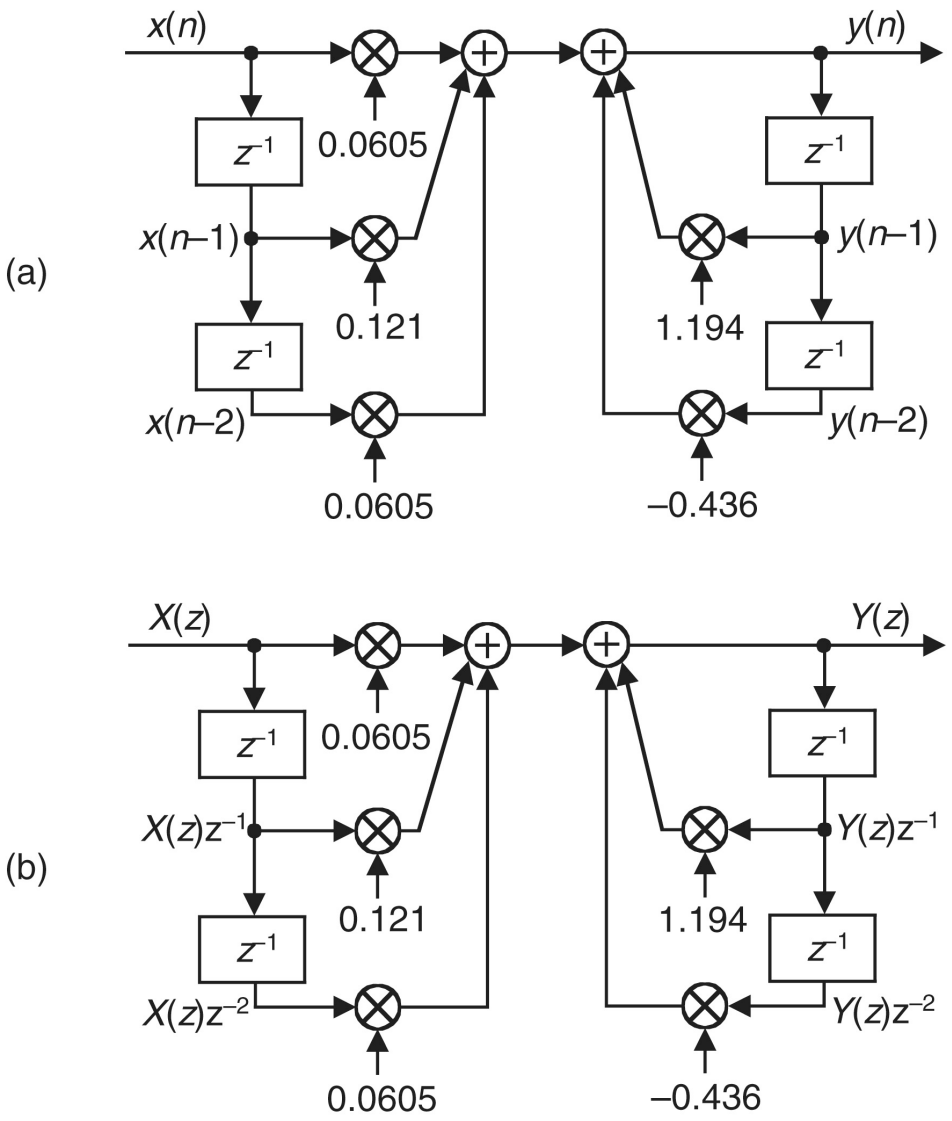

Figure 6–18 Second-order lowpass IIR filter example.

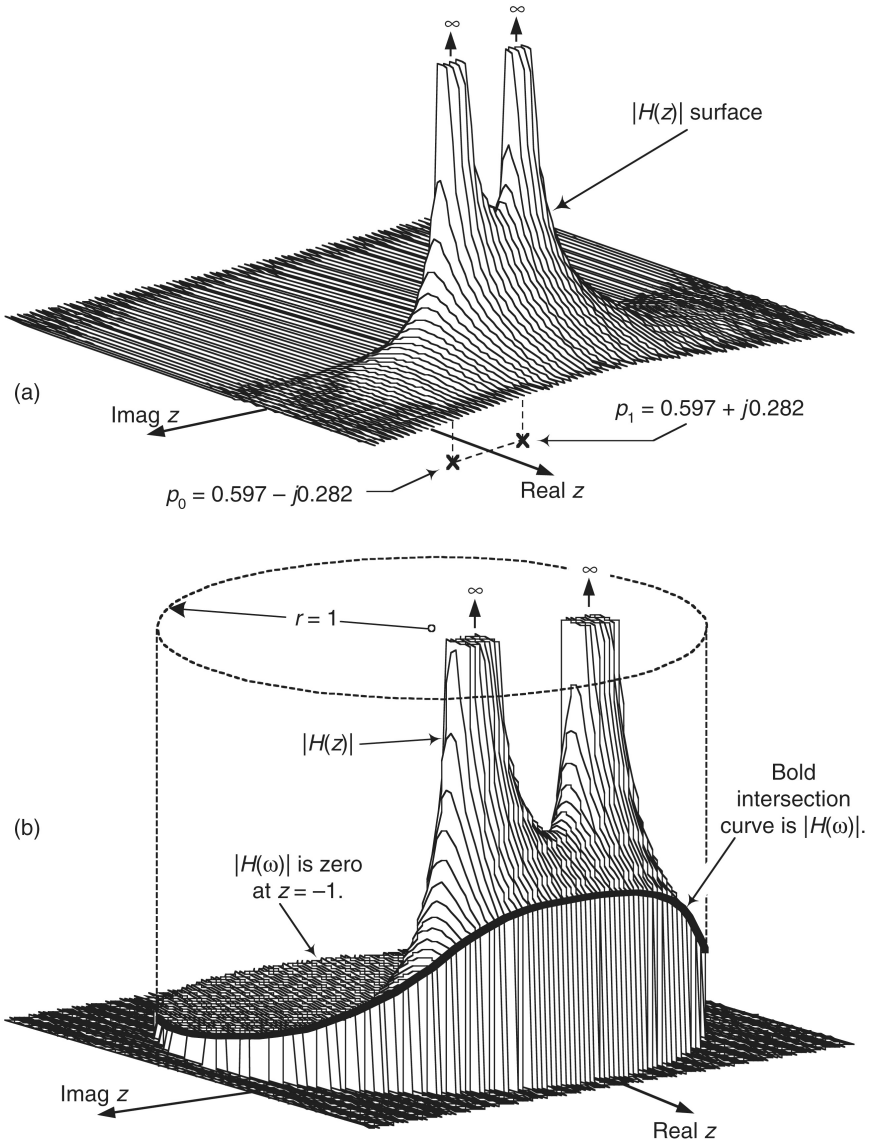

Figure 6–20 IIR filter's $|H(z)|$ surface: (a) pole locations; (b) frequency magnitude response.

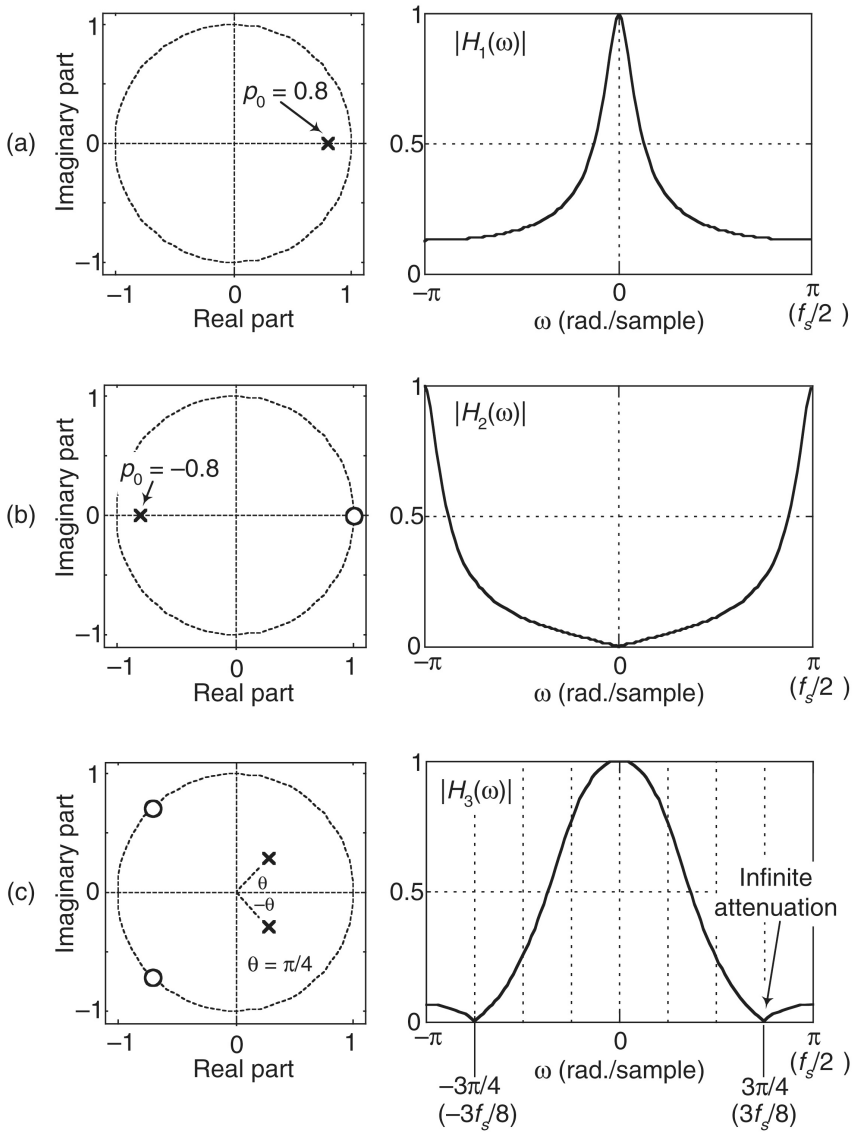

Figure 6–21 IIR filter poles/zeros and normalized frequency magnitude responses.